Robust landscapes of ribosome dwell times and aminoacyl-tRNAs in response to nutrient stress in liver

Cédric Gobet[a,b], Benjamin Dieter Weger[a,b], Julien Marquis[b,1], Eva Martin[b], Nagammal Neelagandan[a], Frédéric Gachon[b,2,3], and Felix Naef[a,3]

[a]Institute of Bioengineering, School of Life Sciences, Ecole Polytechnique Fédérale de Lausanne, Lausanne CH-1015, Switzerland; and [b]Nestlé Research, CH-1015 Lausanne, Switzerland

Edited by Joseph S. Takahashi, The University of Texas Southwestern Medical Center, Dallas, TX, and approved March 9, 2020 (received for review October 18, 2019)

Translation depends on messenger RNA (mRNA)-specific initiation, elongation, and termination rates. While translation elongation is well studied in bacteria and yeast, less is known in higher eukaryotes. Here we combined ribosome and transfer RNA (tRNA) profiling to investigate the relations between translation elongation rates, (aminoacyl-) tRNA levels, and codon usage in mammals. We modeled codon-specific ribosome dwell times from ribosome profiling, considering codon pair interactions between ribosome sites. In mouse liver, the model revealed site- and codon-specific dwell times that differed from those in yeast, as well as pairs of adjacent codons in the P and A site that markedly slow down or speed up elongation. While translation efficiencies vary across diurnal time and feeding regimen, codon dwell times were highly stable and conserved in human. Measured tRNA levels correlated with codon usage and several tRNAs showed reduced aminoacylation, which was conserved in fasted mice. Finally, we uncovered that the longest codon dwell times could be explained by aminoacylation levels or high codon usage relative to tRNA abundance.

protein synthesis | ribosome profiling | tRNA | computational biology

Translation dynamically controls gene expression in processes such as development, the cell cycle, feeding/fasting cycles, and response to stress (1). At least three steps underlie protein synthesis: translation initiation, often thought to be rate limiting; elongation; and termination (2). Recently, however, elongation has emerged as an important layer to fine-tune gene expression (reviewed in ref. 3). Indeed, variations in elongation rates may influence gene expression (4–8), and recent studies showed that alteration of translation elongation rates in cancer cells influences their proliferation and invasion capabilities (9–11).

In unicellular organisms, translation elongation rates are well explained by transfer RNA (tRNA) gene copy number and expression (12, 13). This is also reflected evolutionarily since highly expressed genes are enriched for fast codons with high concentrations of tRNAs (14). Pioneering work in *Escherichia coli* showed that elongation rates are different for the codons GAA and GAG (15), decoded by the same tRNA. This raises the possibility not only that elongation rate is determined by the concentration of tRNAs but that codon–anticodon interactions as well as codon context may play important roles. While the determinants of elongation rates are well studied in bacteria and yeast, much less is known in high eukaryotes.

More recently, the development of ribosome profiling (RP) shed new light on the regulation of translation (16), including in human tissues (17). Notably, the possibility to capture the positions of translating ribosomes on messenger RNAs (mRNAs) (18) fostered the development of quantitative models providing genome-wide insights on key features regulating translation elongation rate (19–22). For instance, the properties of amino acids (23), (aminoacyl-) tRNA availability (24–26), tRNA modifications (27–29), secondary structures of mRNAs (30–32), folding of the nascent chain (33), pairs of codons (34, 35), and sterical interactions with the ribosome exit tunnel (36) were shown to influence the local density of ribosomes on transcripts. While RP studies have brought new knowledge on translation elongation, these were performed mostly in unicellular organisms and have led to divergent results on the determinants of elongation rates, as highlighted in several metaanalyses (20, 37). One reason is that ribosome footprints are sensitive to biases from differences in protocols (38–42), library preparations (22), and data analysis pipelines (43). Consequently, the reported correlations between elongation rates, tRNA abundances, and codon usage (44) show inconsistencies. In addition, while codon usage can be precisely estimated, it remains difficult to measure tRNA concentrations. Indeed, tRNAs exhibit a high degree of modifications and complex secondary structures, which alter cDNA synthesis and biases quantification by high-throughput sequencing (45). Thus, improved methods have been proposed to quantify tRNAs (9, 46–48), as well as tRNA aminoacylation levels (49).

Significance

Protein synthesis is a fundamental and tightly controlled process which allows organisms to respond rapidly to external signals such as nutrient availability or stress conditions. While the initiation step is well studied, the determinants of translation elongation rate on mRNAs are poorly understood, particularly in mammals. Here we combined computational and molecular biology approaches to shed light on the determinants of translation elongation rates and their relationships with aminoacyl-tRNAs in livers of normally fed and fasted mice. We found that the ribosome dwell times in mouse liver depend on codon pairs, were robust to prolonged fasting, and can be explained to some extent by a combination of aminoacyl-tRNA level and codon usage/tRNA balance.

Author contributions: C.G., F.G., and F.N. designed research; C.G., B.D.W., J.M., E.M., and N.N. performed research; C.G. analyzed data; C.G., F.G., and F.N. wrote the paper.

Competing interest statement: C.G., B.D.W., E.M., and F.G. were employees of Nestlé Institute of Health Sciences SA, Lausanne, Switzerland.

This article is a PNAS Direct Submission.

Data deposition: Sequencing data of this study have been submitted to the National Center for Biotechnology Information (NCBI) Gene Expression Omnibus (GEO), http://www.ncbi.nlm.nih.gov/geo/ (accession no. GSE126384). Codes to model DTs and flux from ribosome profiling, as well as, high-quality versions of the figures are available on GitHub: https://github.com/cgob/codonDT_snakemake.

[1]Present address: Lausanne Genomic Technologies Facility, Université de Lausanne, Lausanne CH-1015, Switzerland.

[2]Present address: Institute for Molecular Bioscience, The University of Queensland, Brisbane, QLD 4072, Australia.

[3]To whom correspondence may be addressed. Email: felix.naef@epfl.ch or f.gachon@uq.edu.au.

This article contains supporting information online at https://www.pnas.org/lookup/suppl/doi:10.1073/pnas.1918145117/-/DCSupplemental.

First published April 15, 2020.

Here, to better establish the determinants of translation elongation rate in higher eukaryotes, we combined modeling of ribosome profiling data, codon usage analysis, and (aminoacyl-) tRNA profiling in mouse liver. In particular, we built a genome-wide statistical model that allowed us to estimate elongation rates, notably the contributions of single codons, as well as pairs of codons within and near the ribosome E, P, and A sites. In mouse liver, we found a large dynamic range of codon- and amino acid-specific ribosome dwell times (DTs, defined as the inverse of the elongation rates; *Materials and Methods*). In addition to single-codon effects, we identified codon pairs contributing synergistically to the DTs. In mouse liver, the identified contributions of single-codon and codon pair DTs were remarkably stable along the feeding/fasting cycle and even under conditions of prolonged fasting. Metaanalysis in mammals revealed conserved DTs between mouse tissues and human, which were, however, distinct from those in yeast. Finally, we extended a recent tRNA profiling method (9) to measure (aminoacyl-) tRNA levels in liver of ad libitum (AL) fed and fasted (FA) mice. tRNA levels correlated with codon usage and several tRNAs showed reduced aminoacylation, which was conserved in fasted mice. These data, together with codon usage properties, allowed us to explain some codon specificity in the estimated ribosome DTs.

Results

Modeling Codon-Specific DTs Including Single-Codon and Codon Pair Contributions. Ribosome profiling read counts along transcripts typically show large variations with high and low densities of ribosomes reflecting differential elongation rates. To estimate ribosome DTs in higher eukaryotes from those data, we explicitly fit ribosome profiling read counts on a genome-wide scale, extending previous models (19, 21). Specifically, we consider steady-state translation and additionally assume no ribosome drop-off and low density of ribosomes per transcript. Under this model, the probability of finding a ribosome at a specific position on an mRNA is proportional to a position-independent gene translation flux times a position-dependent ribosome dwell times (19). To investigate how the codon context determines the DTs, we further assumed that DTs depend on position through the codons translated in the E, P, and A sites, as well as surrounding sequences (Fig. S1*A*). In particular, we modeled DTs additively in log-space using single-codon contributions as well as synergistic (nonadditive) contributions from pairs of codons in the E and P (noted E:P), P and A (P:A), or E and A (E:A) sites (Fig. S1 *A* and *B*). Note that the additive log-scale model for the DTs is equivalent to modeling the elongation rates at any given position with an Arrhenius-like rate equation, in which the analogue of the activation energy has both single-codon and codon pair contributions. An inherent property of such approaches is that the DTs cannot be estimated in absolute units but only relative to each other within each site (*Materials and Methods*). Solving this model with appropriate noise distributions for RP count data can be conveniently implemented as a generalized linear model (GLM), which models the expected read counts as gene specific fluxes (gene covariates) multiplied by ribosome DTs (codon covariates) (*Materials and Methods*). The GLM uses the 61 sense codon alphabet and considered positions around the ribosome spanning 40 codons around the E site (Fig. S1 *A* and *B*). To normalize the fluxes per mRNA and attenuate possible technical biases affecting the ribosome DTs, the same model is also applied on RNA-seq when available. Compared to other models predicting ribosome footprint densities (20–22, 31, 37), our approach allows us to determine globally translation elongation parameters, namely, single-codon and codon pair DTs together, as well as fluxes. Moreover, the parameters are all inferred at once from the raw read counts using a negative binomial noise model (Fig. S1 *C–E*) (*Materials and Methods*), which provides a quantitative interpretation of the fitted coefficients, including in particular the identification of synergistic contributions to ribosome DTs.

In Yeast Ribosome DTs Anticorrelate With Codon Usage and Show Codon Pair Interactions. To validate our model, we analyzed two published ribosome profiling datasets in *Saccharomyces cerevisiae* (26, 50), one under normal (wild-type [WT]) (50) conditions and one treated with 3-amino-1,2,4-triazol (3-AT), which inhibits the histidine (His) biosynthesis pathway (26) thereby reducing aminoacylation level of histidine tRNAs. Both datasets used cycloheximide (CHX) only in the lysis buffer.

Our model reproduced raw RP read counts along the transcripts with similar accuracy as previous methods (20–22, 31, 37) in both WT and 3-AT conditions (Fig. S2 *A* and *B*). Interestingly, the estimated dwell times (DTs) in WT exhibited a twofold range at the three E, P, and A sites (Fig. 1 *A* and *B*, *Left*), with some marked slower outliers. For instance, one codon (CCG) for proline (Pro) was markedly slow in the A and P sites, likely due to its wobble decoding. Note that the other three proline codons are also slow, presumably because of slow peptide bond formation, as shown in ref. 51. Arginine (Arg) showed long DTs in all three sites. In fact, some Arg codons also showed slightly longer DTs in the upstream sequence, highlighting possible interactions of this positively charged amino acid with the ribosome exit tunnel (Fig. S2*C*). On the other hand, codons for isoleucine (Ile), leucine (Leu), and valine (Val) were the fastest in the A site (Fig. 1 *A* and *B*, *Left*).

We found that the shortage of His in the 3-AT condition resulted in lengthened DTs in the P and A sites for both His codons (CAC and CAT) (Fig. 1 *A* and *B*, *Right*), confirming the sensitivity of the estimated DTs. Interestingly, outside the E, P, and A sites, DTs showed a dependency on His codons at around 30 nucleotides (positions 11 and 12) downstream of the P site (Fig. S2*C*), reflecting queued ribosomes (disomes) behind His codons (26). Moreover, the DTs also displayed signatures of technical biases. Notably, the high variation in DTs at position −4, coinciding with the most 5′ nucleotide of the insert, was previously shown to reflect biases in library preparation (Fig. S2*C*) (reviewed in ref. 52).

To further validate the biological relevance of our DTs, we compared ribosome DTs in WT condition with codon usage weighted by mRNA translation levels (i.e., normalized RP read counts), to take into account condition-specific demands in codons. Interestingly, we found high negative correlations ($R^2 = 0.565$ and $R^2 = 0.495$) between the codon usage and the DTs at the A and P sites (Fig. 1*C*). This observation suggests an evolutionary pressure to enrich for fast codons in highly expressed genes, and conversely.

In addition to the single-codon DTs, we probed whether pairs of codons in the ribosome sites synergize by analyzing interaction terms (E:P, P:A, and E:A) (Fig. S2*D*). We compared these predicted DTs with a GFP-reporter experiment in yeast probing for pairs of codons that inhibit translation (35). Indeed, the experimentally determined inhibitory pairs exhibited long predicted DTs at the P and A or E and P ribosome sites (Fig. 1 *D–F*). While for these pairs the single-codon DTs were already long, the synergistic interaction terms clearly prolonged them (Fig. 1 *D* and *E*). Interestingly, although the E:P and P:A interactions were not correlated overall, the inhibitory pairs stood out as showing large DT contributions in both the E:P and P:A (Fig. 1*F*). Globally, the P:A interaction matrix was sparse and not highly structured but revealed large values and spread for the pairs involving codons for Arg or Pro (Fig. S2*D*). Thus, our model of RP data is sufficiently sensitive to identify subtle properties of ribosome DTs, such as codon-specific and codon pairs contributions, and signatures of sequences outside of the E, P, and A sites.

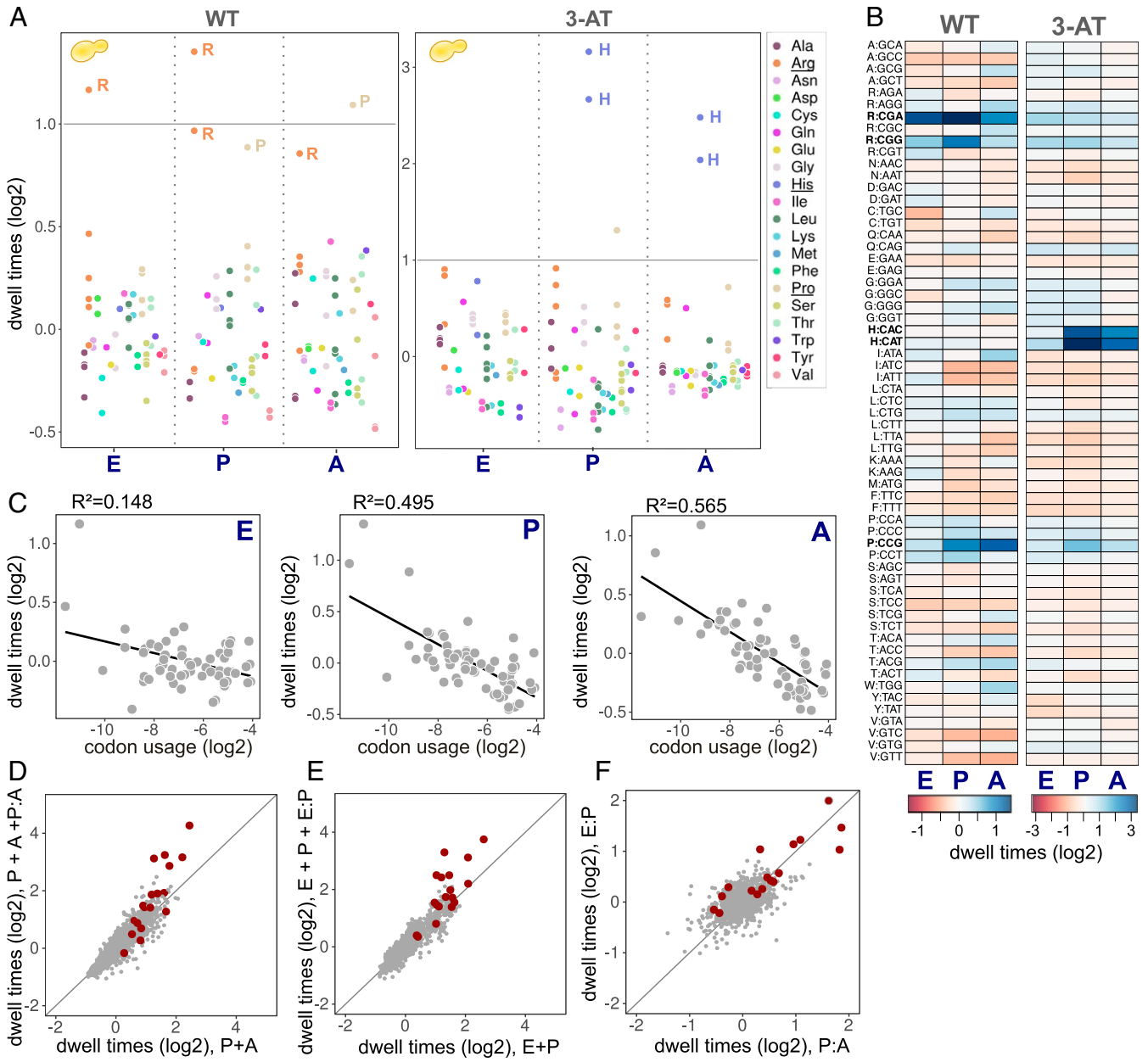

Fig. 1. In yeast, ribosome DTs anticorrelate with codon usage and show codon pair interactions. Panels for the single-codon DTs are retrieved from the fit with the P:A interaction. (*A*) DTs (log2, mean centered per site) for the 61 sense codons in the two conditions (WT [*Left*] and 3-AT [*Right*]) for the E, P, and A sites. Codons are colored according to amino acids. DTs with $p >= 0.05$ are not shown. (*B*) Heat map representation of *A*. Here DTs with $p >= 0.05$ are set to 0. Relatively fast and slow interactions are shown in dark red and dark blue, respectively. (*C*) Codon usage weighted by mRNA translation levels (normalized RP read count) correlates with the codon DTs for the E, P, and A sites. Black line shows linear fit. (*D*) DTs (log2) for codon pairs. Total codon pair DTs (P + A + P:A, i.e., including the interactions P:A) versus the contributions from the single-codons (P + A). Red indicates pairs described as inhibitory in ref. 35. (*E*) DTs (log2) for codon pairs. Total codon pair DTs (E + P + E:P, i.e., including the interactions E:P) versus the contributions from the single codons (E + P). Red indicates pairs described as inhibitory in ref. 35. (*F*) P:A (log2) versus E:P (log2) interactions for all codon pairs.

Single-Codon and Codon Pair DTs in Mouse Liver Cluster by Amino Acids. Determinants of translation elongation are less studied in mammals. We and others have previously shown that feeding/fasting cycles can regulate translation initiation in mouse liver via well-described mechanisms, notably through mTOR and GCN2 related nutrient sensor pathways (53, 54). Here we aimed to extend this analysis to the level of DTs, in particular to assess whether perturbed amino acid pools during low nutrient availability can alter DTs. Therefore, we applied the above model to our previous 84 ribosome profiling samples harvested in WT and circadian clock deficient mice (*Bmal1* KO) every 2 to 4 h around the 24-h d, including four biological replicates (53). As for yeast, our model faithfully captured raw RP read counts along transcripts, as reflected by a previously used correlation metric (Fig. S3 *A* and *B*). Remarkably, DTs were very stable across all samples, showing high biological reproducibility and no time or circadian clock-dependent changes (Fig. S3 *C–E*), as opposed to rhythmic gene-specific translation efficiencies (53). Therefore, for the following analyses of DTs, we averaged them over all of the 84 samples.

DTs for the E, P, and A sites showed biologically significant codon and amino acid specificity (Fig. 2 *A* and *B*). DTs were

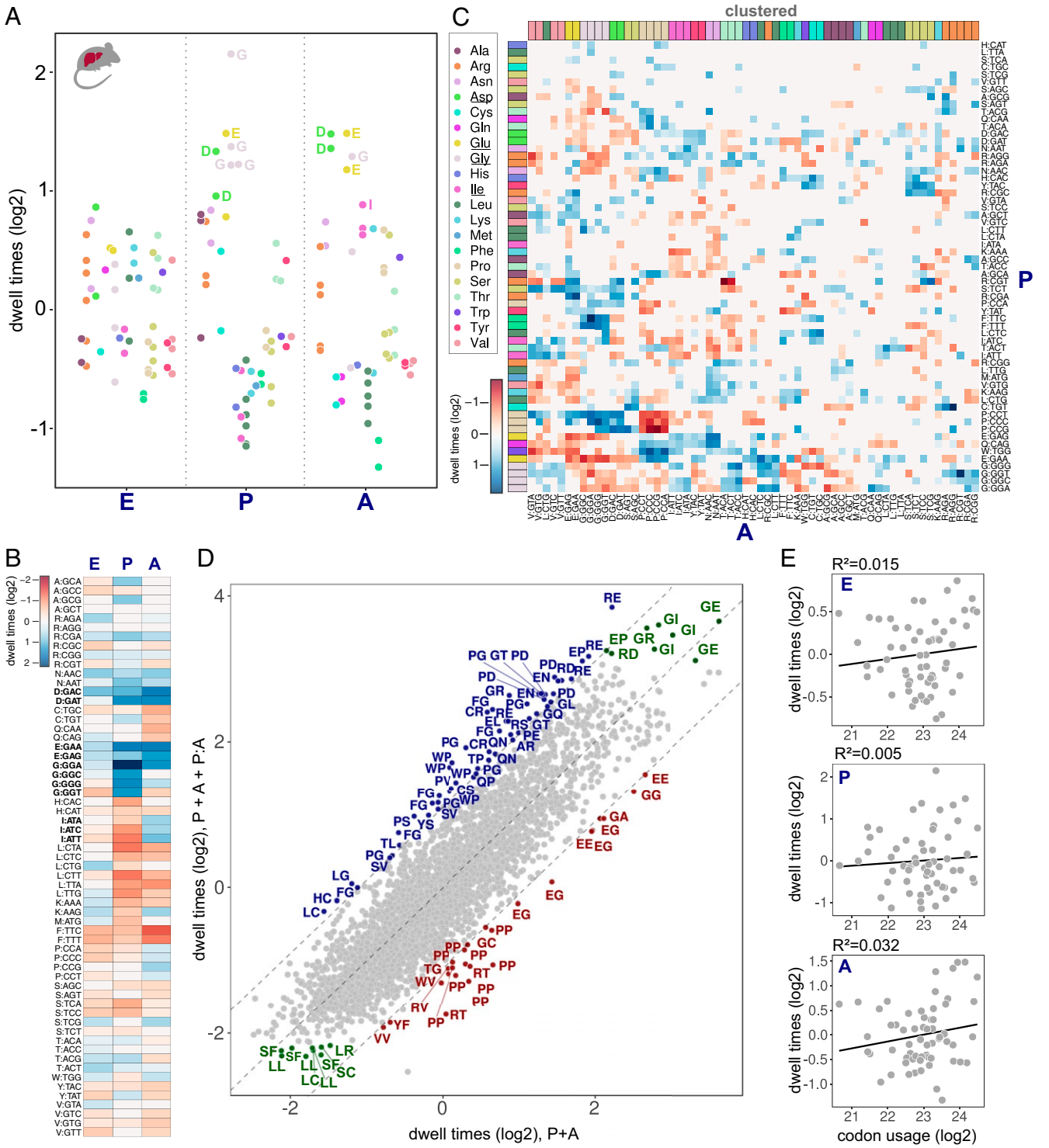

Fig. 2. Single-codon and codon pair DTs in mouse liver cluster by amino acid. Single-codon DTs are retrieved from the fit with the P:A interaction. (*A*) DTs (log2, mean centered per site) for the E, P, and A sites averaged over the 84 samples in mouse liver. Codons are colored according to amino acids. DTs with $p >= 0.05$ are set to 0. (*B*) Heat map representation of *A*. DTs with $p >= 0.05$ are set to 0. Fast and slow DTs (relative to the mean) are shown in dark red and dark blue, respectively. (*C*) Interaction matrix for the pairs P:A (log2). Codons are colored according to amino acids. Codons in both sites are hierarchically clustered (euclidean distance matrix, complete linkage algorithm). Fast and slow interactions are shown in dark red and dark blue, respectively. (*D*) DTs (log2) for codon pairs. Total codon pair DTs (P + A + P:A, i.e., including the interactions P:A) vs. the contributions from the single codons (P + A). Pairs with interactions > 1.1 or < -1.1 are annotated and colored in blue and red, respectively. Top 10 slowest and fastest pairs are colored in green if not already depicted. (*E*) Codon usage weighted by mRNA translation levels (normalized RP read count) does not correlate with codon DTs for the E, P, and A sites. Black line indicates linear fit.

strikingly different from those in yeast and exhibited a larger dynamic range (Fig. 2 *A* and *B*). In particular, the P and A sites revealed nearly 10-fold range in DTs between the fastest and slowest codons, while DTs in the E site were more tightly distributed (Fig. 2 *A* and *B*), presumably reflecting that the DTs are primarily sensitive to aminoacyl-tRNA availability (A site) and peptide bond formation (P-A sites). While DTs in the P and A site were overall more strongly correlated to each other than with the E site, DTs also showed clear site specificity (Fig. 2 *A* and *B*). For instance, the four codons for Glycine (Gly) had long DTs in the P site; however, the Gly GGT codon was among the fastest in the E and A sites, while the GGA codon was markedly slow in the A site. Strikingly, all three Ile codons had long DTs in the A site but very short DTs in the P site (Fig. 2 *A* and *B*). For the negatively charged glutamate (Glu) and aspartate (Asp), all of their codons showed long DTs in the P and A sites (Fig. 2 *A* and *B*). Considering a larger window around the ribosome revealed that P and A sites, followed by the E site, showed the largest contributions to DTs (Fig. S4*A*). The detected signals at the −4 and +6 positions reflect known ligation biases during the library preparation (52). Upstream and downstream sequences outside the (−4, +6) interval slightly contribute (Fig. S4*A*), while codons in the vicinity of the ribosome (−3, −2, −1 and +3, +4, +5) exhibited considerable variations in DTs and were correlated between both sides.

We found that codon pair DTs have a significant influence on translation elongation in mouse liver, with P:A interactions showing the widest dynamic range, followed by E:P and E:A (Fig. S4*B*). The estimated interaction matrices are not symmetric, showing codons or amino acid specificity at the respective ribosome sites (Fig. 2*C* and Fig. S4*C*). Intriguingly, the P:A matrix highlighted a striking clustering by amino acid for the A site (Fig. 2*C*), while E:P interactions clustered by amino acid in the P site (Fig. S4*C*). This suggests that P:A codon pair DTs are determined by amino acids through their influence on the peptide bond formation. The clustering by amino acid was corroborated by a model selection analysis on the 84 samples, where the alphabet for the DT regression coefficients was taken as either the 20 natural amino acids or the 61 sense codons (Fig. S4*D*). While the preferred alphabet was overall that of the codons, the model with amino acid coefficients at the A site for the P:A interaction was preferred to all of the other models (Fig. S4*D*). In the case of the E:P interaction, the amino acid alphabet in the P site was considered as the best model (Fig. S4*D*). Overall, models including the site interactions were preferred to the reduced models, emphasizing the importance of codon pair interactions in determining ribosome DTs in mouse liver. The P:A matrix revealed strong positive interactions (lengthening the DTs) for pairs of bulky (Pro, tryptophan [Trp], and phenylalanine [Phe]) or achiral (Gly) (Fig. 2 *C* and *D*) amino acids. Surprisingly, the known stalling pair Pro–Pro showed the largest negative interaction (Fig. 2 *C* and *D*), possibly related to eIF5A activity which is known to facilitate otherwise slow peptide bond formation for such pairs (55). Overall, these interactions contributed to the total codon pair DTs for the P and A site by a factor larger than 2 for about 100 pairs (Fig. 2*D*). Summing the single-codon and codon pair contributions showed that the amino acid pair glycine–isoleucine was represented by multiple combinations of codons in the top 10 overall slowest pairs (Fig. 2*D*). Similarly, the leucine–leucine pair was frequent among the fastest codon pairs (Fig. 2*D*). The E:P matrix showed that pairs involving the amino acids Gly, Asp, Asparagine (Asn), and Pro in the P site lengthened the total codon pair DTs (Fig. S4*C*).

Unlike in yeast (Fig. 1*C*), ribosome DTs did not correlate with codon usage in mouse liver (Fig. 2*E*), arguing for different evolutionary pressure on translation efficiency.

Ribosome DT Patterns in Liver Are Stable Under Prolonged Fasting. The above analysis showed highly robust DTs between liver samples collected during the normal feeding (night)/fasting (day) cycle (Fig. S3 *C*–*E*). To probe whether translation elongation rates are sensitive to longer periods of fasting, we performed ribosome profiling experiments in mice fed either ad libitum (AL) or fasted (FA) for up to 30 h (Fig. 3*A*). Since the enrichment in ribosome footprints can be sensitive to RP protocols (56), we here used a small RNA-Seq protocol with random adapters (UMI) to reduce possible ligation biases and to control for PCR duplicates. Moreover, as ribosome dynamics and DTs are affected in ribosome profiling experiments with cycloheximide (CHX) in yeast (40, 57), we tested conditions without CHX in the lysis buffer.

First, we validated the effect of prolonged fasting by analyzing polysome profiles and differential ribosome profiling signals between AL and FA (Fig. 3 *B* and *C*). Polysome profiles of mouse liver after 30 h of fasting showed a massive shutdown of global protein synthesis. Indeed, fractions corresponding to monosomes and free ribosomal subunits were largely increased, while polysome fractions were reduced (Fig. 3*B*). In the RP analysis, genes related to the Peroxisome Proliferator-Activated Receptor α (PPARα) pathway and to fatty acids oxidation were upregulated in FA, presumably to provide the energy needs (Fig. 3*C*). On the contrary, genes related to lipid biosynthesis were downregulated in FA (Fig. 3*C*), suggesting that animals switched from glucose to fatty acid metabolism in FA, as already described (58). Moreover, *Mat1a*, *Asl*, and *Got1* related to amino acid biosynthesis were upregulated in FA (Fig. 3*C*), presumably in response to perturbed amino acid homeostasis. We probed whether the perturbed metabolic state in FA might lead to differential codon usage (25). Strikingly, when considering the codon usage bias in WT and FA animals, we found that most of the codons with a G or C nucleotide at the third position (GC3) were enriched in up-regulated transcripts in FA, while codons with an A or T nucleotide were underrepresented (Fig. S5*A*).

The ribosome profiling data in the new conditions showed a typical trirepeat nucleotide pattern (Fig. 3*D*), confirming the presence of bona fide translating ribosomes in the FA samples, as well as in samples without CHX (NOCHX). In addition, the modified library preparation improved the goodness of the fits. Indeed, correlation coefficients introduced above (Fig. S3 *A* and *B*) were now higher (Fig. S5 *B* and *C*). While the FA samples showed a reduced dynamic range in the DTs, presumably due to increased signal to noise related to the global decrease in translation levels (Fig. 3*B*), single-codon DTs in the AL and FA conditions showed no relative differences (Fig. 3*E* and Fig. S5 *D* and *E*). The fact that the dwell times are unaffected after 30 h of fasting shows a strong resilience of the tissue to amino acid deprivation and suggests compensatory mechanisms, such as a global decrease of translation initiation, to maintain the aminoacyl-tRNA pool (24). Note that the dwell times are not changed between the CHX or NOCHX conditions (Fig. S5*D*), indicating that use of CHX in the lysis buffer does not distort translation dynamics. Codon pair DTs were also very similar across conditions (Fig. S5*E*).

Metaanalysis Reveals Conserved Ribosome DTs in Mammals. To further compare the estimated ribosome DTs, we analyzed published ribosome profiling datasets in mouse liver (H, Howard et al.) (59), mouse kidney (CS, Castelo-Szekely et al.) (60), and the human liver cell line Huh7 (L, Lintner et al.) (61). Despite differences in library preparation protocols (*Materials and Methods*), single-codon DTs at the A site were highly correlated between the mammalian datasets ($0.48 < r < 0.96$), including in different tissues (kidney) and human cells (Fig. S6 *A* and *B*). However, the mammalian DTs were markedly different from those in yeast

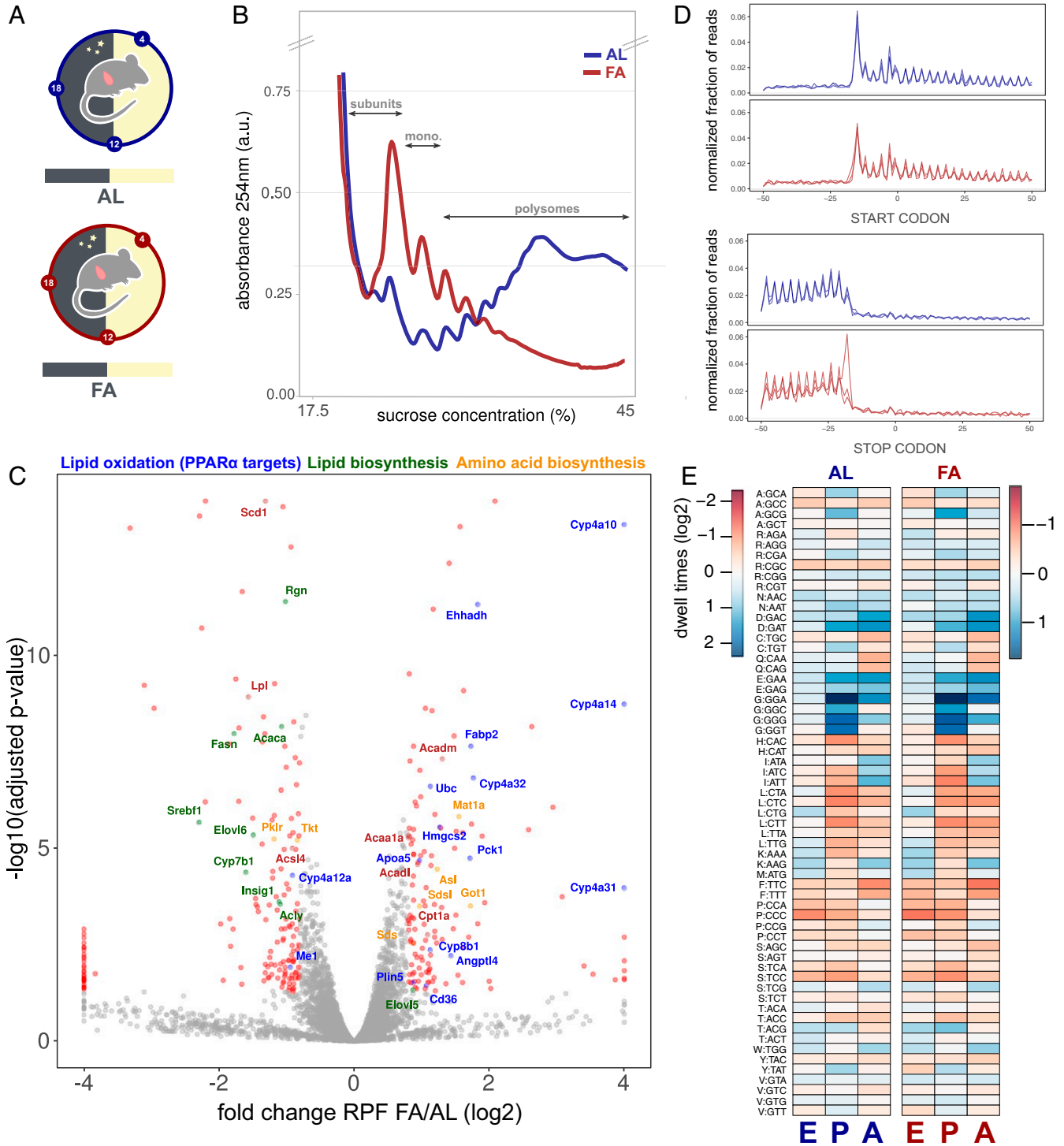

Fig. 3. Ribosome DTs are not affected in fasted mice and without cycloheximide. Single-codon DTs are retrieved from the fit with the P:A interaction. (*A*) Livers from mice fed AL or FA were harvested at ZT4, ZT12, and ZT18 (fasting of 16, 24, and 30 h, respectively). Ribosome profiling was performed without cycloheximide (CHX) in the lysis buffer. (*B*) Polysome traces (absorbance at 254 nm) for liver samples at ZT18 in AL and FA conditions. The relative positions of the ribosome subunits, monosomes, and polysomes are indicated. (*C*) Differential expression of ribosome profiling signals between AL and FA (*Materials and Methods*). Benjamini–Hochberg adjusted *P* values (−log10) are plotted against averaged log2 fold change between FA and AL. Genes with *P* values of 0.01 and absolute log2 fold change > 1 are annotated and colored. Blue indicates genes in the KEGG PPARα signal pathway, green indicates KEGG and GO term lipid biosynthesis, orange indicates KEGG amino acid biosynthesis, and brown indicates genes related to more than one GO term. (*D*) Normalized fractions of reads of length 32 around the start and stop codons in a window of 100 nucleotides, genome-wide. Dark blue indicates AL/NOCHX; dark red indicates FA/NOCHX. (*E*) DTs (log2, mean centered per site, heat map) for the E, P, and A sites in AL/NOCHX and FA/NOCHX. Codons are ordered by amino acid. Fast and slow DTs (relative to the mean) are shown in dark red and dark blue, respectively.

(20). Note that the relative contribution to the DTs from the E, P, and A sites vs. that from surrounding sites, in particular at positions −4 and +6, differed depending on the protocols (Fig. S6 *C* and *D*). Similar potential biases have been reported previously (56). Here we found that protocols without cDNA circularization showed highest signals in the P and A sites, presumably reproducing ribosome dynamics more faithfully (Fig. S6 *C* and *D*). Moreover, this was also reflected in the codon pair DTs (P:A), which were more consistent across experiments with that protocol (Fig. S6*E*).

Together, this metaanalysis highlighted how different library preparations lead to damped RP signals in the A and P sites for some protocols and showed that the codon DT patterns are conserved between mouse tissues and mammalian species and different from yeast.

(Aminoacyl-) tRNA Profiles Are Conserved in Fed and Fasted Mice. We next asked whether the estimated DTs can be linked with tRNA abundances or loading levels, which is poorly studied in higher eukaryotes (44). The chemical modifications and secondary structure of tRNAs render them difficult to quantify. A recent hybridization method combined with sequencing, which controls specificity using left/right probes and a stringent splint ligation step, allows us to bypass the cDNA synthesis to quantify tRNA levels (9). To measure tRNA abundances and assess possible links with ribosome DTs in mouse liver, we first adapted and optimized this method to target all annotated mouse tRNAs (Fig. S7*A*). Moreover, we quantified (aminoacyl-) tRNAs using NaCl or sodium periodate (62) to separate total and charged tRNAs by selective biotinylation of 3′-ends (Fig. S7*A*). This way, we aimed to quantify the tRNA pools available for elongation in the ribosome A site.

tRNA molecules are encoded by a large number of genes. Therefore, we designed 303 DNA probe pairs (left and right) to target all mouse tRNA sequences in the *GtRNAdb* database (63) (Fig. S7*A*). Our modified protocol yielded a high proportion of correct ligations between left and right probes, showing target specificity for tRNAs (Fig. S7*B*) and validating the specificity and the efficiency of DNA ligases in our protocol (Fig. S7 *C* and *D*). Indeed, mapping of the sequencing reads to all possible combinations (303^2) of left and right probes showed that more than 75% of ligated products belonged to tRNA genes of the same codon (Fig. S7*B*), and even 95% were from probe pairs that could be assigned to one codon with high confidence (Fig. S7*B* and *Materials and Methods*).

We measured relative tRNA abundance on mouse livers from the same samples as those used for the ribosome profiling (Fig. 3*A*). Specifically, we quantified the total tRNA (control, NaCl) and the (aminoacyl-) tRNA (sodium periodate, $NaIO_4$) relative abundances from the same pieces of liver in two replicates in the AL and FA conditions, at three different times during the day (ZT04, ZT12, and ZT18) (Fig. 4*A* and *Materials and Methods*). tRNA abundances were highly reproducible (Fig. S7*E*), exhibited a large dynamic range (Fig. 4*B*), and were positively correlated with PolIII ChIP-Seq data in mouse liver (64) (Fig. S7*F*). tRNA levels for amino acids encoded by four synonymous codons (four-codon box) were represented by one dominant highly expressed isoacceptor with a U at the wobble position 34 (e.g., UGC/Ala, UGG/Pro, UCC/Gly, UAC/Val, and UGT/Thr) (Fig. S8*A*). The tRNA levels showed only small variations over the biological conditions, except for mitochondrial tRNAs (Fig. S8*B*). Principal component analysis (PCA) on the four conditions (i.e., NaCl/AL, NaCl/FA, $NaIO_4$/AL, and $NaIO_4$/FA) showed a clear separation between the control (total tRNA) and periodate conditions (aa-tRNA) (Fig. 4*C*), indicating differential loading of the tRNAs. Similarly to the stable DTs (Fig. 3*E*), the AL and FA samples were indistinguishable at the total tRNA and (aminoacyl-) tRNA levels (Fig. 4 *C* and *D*), indicating no imbalance of tRNA charging in prolonged fasting. This observation suggests compensatory mechanisms to keep translation elongation rates unchanged, such as decreased total translation which limits aminoacyl-tRNA depletion, or activation of autophagy to replenish the amino acid pool (24).

Finally, we found that some codons for Asn, Asp, and Ile were lowly aminoacylated, independently of the feeding state (Fig. 4*D* and Fig. S8*C*). Strikingly, these same codons were found to exhibit the slowest DTs in the A site (Fig. 2).

Relationship Between (Aminoacyl-) tRNA Levels, Codon Usage, and Dwell Times. We next investigated whether variations of single-codon DTs and codon usage could be explained by the available tRNA pools. We found a positive correlation ($R^2 = 0.22, p = 1.2e-4$) between codon usage and our measured tRNA levels in mouse liver (Fig. 5*A*). This modest but statistically significant correlation is in the range of previously reported values (65–67) and indicates that other factors drive codon bias in higher eukaryotes (67).

Our analysis also highlighted codons with high or low demand (codon usage) compared to the supply (tRNA levels), as quantified by the codon balance (68) (Fig. 5*A*). Notably, Glu codons are in high demand, showing the most negative balance.

DTs in the A site did not exhibit a simple correlation with tRNA abundances (Fig. 5*B*), nor with the codon balance (Fig. 5*C*). However, several codons with the slowest DTs in the A site stood out as having either negative codon balance or low aminoacylation levels. For instance, the slow DTs for Glu codons (Fig. 5*C*) may well result from their high codon demand and low tRNA levels, hence limiting tRNA availability at the A site. Overall, DTs in the A site were not clearly correlated with tRNA aminoacylation levels (Fig. 5*D*). However, codons for Asp, Asn, and Ile, which have particularly lowly charged tRNAs, coincided with some of the slowest DTs in the A site (Fig. 5*D*). We therefore included several of those effects in a linear model, which uncovered that a linear combination of tRNA aminoacylation levels and codon balance captures a significant portion of variation in the A site DTs, particularly the long DTs for Glu, Asp, Asn, and Ile codons (Fig. 5*E*).

Discussion

We extensively modeled RP datasets and uncovered single-codon and codon pair DTs determining translation elongation rates in mammals. These DTs were highly stable across all conditions tested. In parallel, we quantified (aminoacyl-) tRNA levels in mouse liver and identified features regulating elongation, such as aminoacylation levels and the balance between tRNA levels and codon usage.

The validations in yeast showed that our model was sensitive at detecting changes in codon-specific DTs and highlighted mainly Arg and Pro as slow in the A and P sites. These amino acids are known for their slow peptide formation or sterical interactions with the ribosome (69, 70). A significant negative correlation was observed between DTs and codon usage, reflecting natural selection for fast codons in highly translated genes. While this relationship has been described (37, 71), the found correlation is, to our knowledge, the highest reported. Moreover, our analysis confirmed recently identified inhibitory pairs (35) and deciphered their synergistic effect in addition to the site-specific contributions. We showed that the inhibitory pairs lengthened DTs both in the E:P and P:A positions, highlighting potentially slow translocation of the pair due to a particular mRNA conformation, as described recently (72).

In mouse liver, DTs differed from yeast, showing a larger spread and higher complexity. Remarkably, DTs were very similar between different tissues, species, and RP protocols.

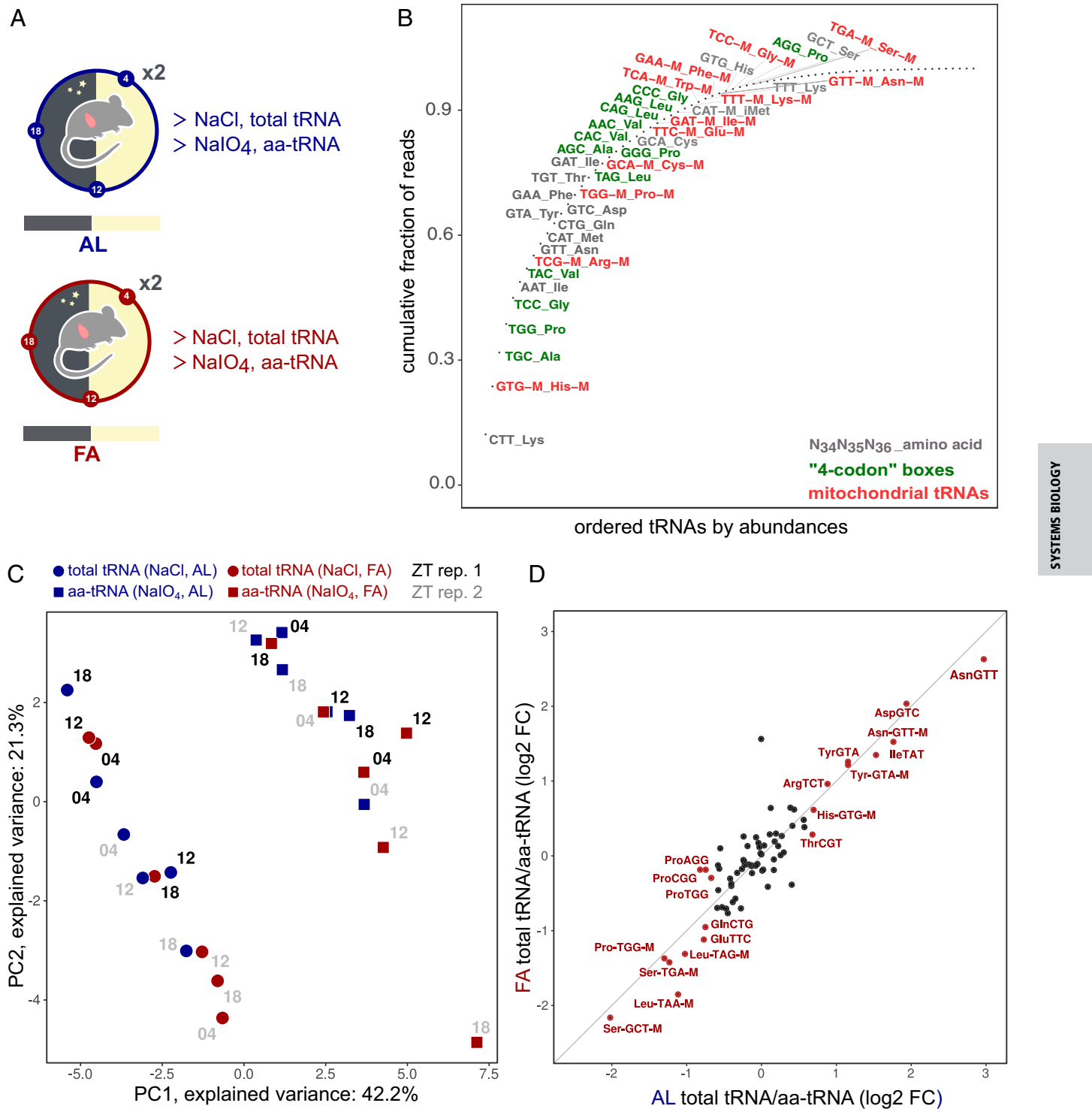

Fig. 4. (Aminoacyl-) tRNA profiling in AL fed and FA mice. (*A*) Mice fed AL or FA were killed at ZT4 (fasting duration, 16 h), ZT12 (24 h), and ZT18 (30 h) and livers were harvested. Each sample was treated with NaCl and sodium periodate ($NaIO_4$) to measure total tRNA and aminoacyl-tRNA (aa-tRNA) relative levels, respectively. (*B*) Cumulative fraction of reads for each tRNA, ordered by abundances in AL/NaCl samples. Anticodons and amino acids are indicated for the 50 first codons. Green indicates four-codon box amino acid; red indicates mitochondrial tRNAs. (*C*) PCA of the total and aa-tRNA abundances in AL and FA samples (log2). PC1 and PC2 explain 42.2 and 21.3% of the variance, respectively, and separate NaCl from $NaIO_4$ treatment. NaCl/total tRNA (circle), $NaIO_4$/aa-tRNA (square), AL (blue), FA (red). ZT is shown beside the points for replicate 1 (black) and replicate 2 (gray). (*D*) Ratio of tRNA abundances (log2 fold change, averaged over the time points) between the total tRNA and aa-tRNA for AL fed vs. FA mice (significant changes in red [$p < 0.05$]). No tRNA showed a significant difference between AL and FA (i.e., fell out of the diagonal) as the clear outlier (Cys-tRNA ACA) showed large interanimal variability.

Moreover, the DTs were consistent with a peptide motif enriched in stalled ribosome sites in mouse embryonic stem cells (mESCs) (73).

We found that the smallest and achiral amino acid Gly exhibited very long DTs (in the A and P site) with different magnitudes between the isoacceptors and tissues (i.e., liver vs. kidney).

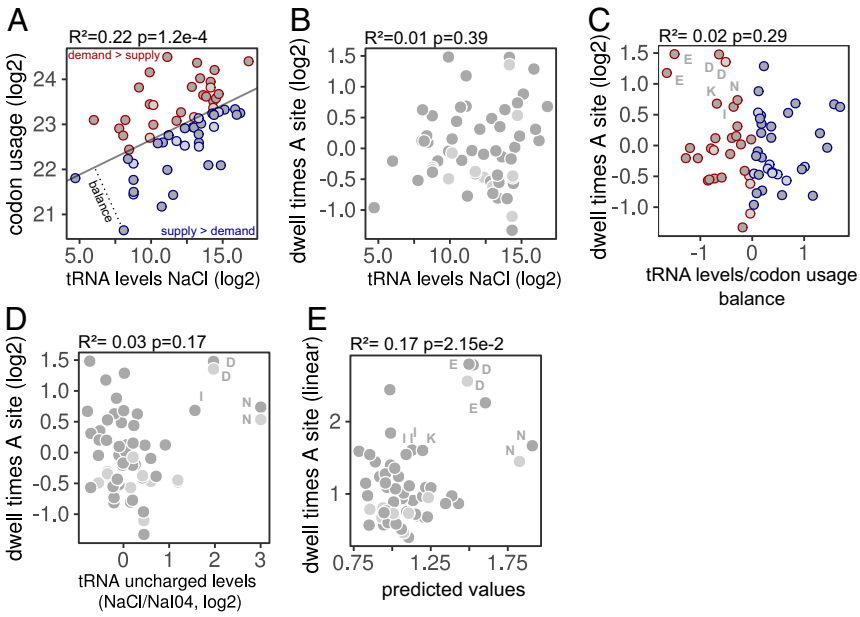

Fig. 5. Relationship between (aminoacyl-) tRNA levels, codon usage and DT. (*A*) Correlation ($R^2 = 0.22$, $p = 1.2e-4$) between codon usage weighted by mRNA translation levels (log2) and normalized total tRNA (NaCl) read count for each codon (log2, UMI, averaged over the AL samples). The gray line shows the first principal component (PC). Orthogonal distance to the PC reflects the balance between tRNA supply and demand. Codons with positive or negative balance are colored in blue and red, respectively. Codons are assigned to their canonical tRNAs (dark grey) or to wobble tRNAs (light grey) where appropriate (*Materials and Methods*). (*B*) DTs in the A site (log2) vs. tRNA levels (NaCl, log2) averaged over the AL samples ($R^2 = 0.01$, $P = 3.9e-1$). (*C*) Correlation between tRNA levels/codon usage balance and DTs in the A site (log2) averaged over the AL samples ($R^2 = 0.02$,$P = 2.9e-1$). (*D*) Correlation between tRNA uncharged levels (NaCl/$NaI0_4$, log2) and DTs in the A site (log2) averaged over the AL samples ($R^2 = 0.03$, $P = 1.7e-1$). (*E*) Correlation ($R^2 = 0.17$, P = 2.15e − 02) between estimated and predicted DTs in the A site. Prediction uses a linear model with the balance and uncharged levels, in linear scale, as explanatory variables. In *C–E*, annotations refer to one-letter amino acid.

Interestingly, in bacteria, Gly codons are slow, although this effect is still difficult to separate from Shine–Dalgarno (SD) dependent stalling (74) or protocol artifacts (75). As mammals do not use an SD mechanism, our results support an alternative mechanism, such as slow codon–anticodon pairing (76) or slow peptide bond formation. Pioneering work in *E. coli* suggested that Gly-tRNAs adopt a particular conformation due to the U nucleotide in position 32 and that unmodified U_{34} on $tRNA^{Gly}_{UCC}$ could decode the four Gly codons [a pairing known as superwobbling (77)] but with low efficiency (reviewed in ref. 76). While this mechanism was shown in unicellular organisms, our tRNA profiling found $tRNA^{Gly}_{UCC}$ as the major Gly isoacceptors and one of the most abundant tRNAs in mouse liver. Further work may indicate whether superwobbling can occur in the liver.

The DTs for the acidic amino acids (Asp and Glu) were among the slowest. Glu showed a particularly low balance of tRNA levels/codon usage, and Asp tRNA was lowly charged. This could lead to a shortage of tRNA availability and ribosome stalling (24). As their codons share the same first two bases, competition with near-cognate tRNAs (28) or pairing inefficiency due to the wobble mechanism could also explain the long DTs. Indeed, slower elongation would allow higher precision in codon–anticodon discrimination (78).

Isoleucine codon DTs were slow in the A site while fast in the P site. Remarkably, the isomeric Leu codons were the fastest in the P and A sites, suggesting a structure-independent mechanism. Indeed, we showed that Ile-tRNAs were lowly aminoacylated, reducing Ile availability on the A site, but other explanations are possible. For instance, since Ile is decoded by three different codons, a suitable pairing mechanism such as inosine or U34 modifications could be used to avoid pairing of the fourth near-cognate codon (Met) and therefore increase the DTs (79).

One of our main findings concerned the contributions of codon pair interactions toward DTs, mainly at the P and A sites. At these positions, the ribosome catalyzes the peptide bond formation between (aminoacyl-) tRNA in the A site and peptide-tRNA bound to the P site. Our analysis revealed that the identity of the amino acid in the A site (acceptor), and not the codon, was the best descriptor of those codon pair interactions. Pairs including bulky amino acids or Gly in the A site were slow, highlighting their potential inefficiency in peptide bond formation. Interestingly, the DT for Pro–Pro pairs, known to slowly form peptide bonds (51), was markedly reduced by the interaction. This observation probably shows the role of eIF5A in resolving this stalling motif. On the other hand, Gly, Asp, and Glu, which were slow in our analysis, were shown to require eIF5A for their efficient translation (80, 81).

Other features not included in the model, and which are independent of the codon identity, might regulate translation elongation. A high number of liver proteins are secreted and thereby translated by ribosomes bound to the endoplasmic reticulum via the interaction of signal recognition particles with the nascent peptide chain. These interactions are known to stall the ribosomes; however, as these appear to be codon independent, we did not detect them in our analysis (31). In addition, chaperone proteins interacting with the nascent peptide can influence cotranslational folding and subsequent ribosome density on mRNAs (82). The model could also be further extended by including RNA secondary structure and modifications, pseudoknots acting as ribosome roadblocks, and slippery sequences inducing frame shifting (21, 31, 83, 84). Recent studies have described ribosome collisions and their relationships with recruitment of ribosome quality control and degradation pathways (85, 86). While these events could happen frequently in liver, and thereby bias position-dependent estimation of DTs from standard ribosome profiling, a recent study probing the

determinants of collided ribosomes in mouse liver showed similar codon dependencies at pausing sites, compared to our DTs (87).

While we found a striking correlation between DTs and codon usage in yeast, the same did not hold in mammals. This suggests that biased codon usage in mammals reflects more complex evolutionary forces, such as mutation driven GC bias (67). Nevertheless, the measured tRNA abundances in liver showed signatures of adaptation since tRNA levels correlated with the codon usage. These correlations extended previous results at the transcription level or in highly expressed genes (65, 67).

Surprisingly, tRNA loading and DTs were largely unaffected by prolonged fasting. While several studies in cell lines showed that decreasing amino acids in culture media leads to decreased (aminoacyl-) tRNA availability and therefore increases ribosome stalling (24, 62), these studies also showed that upon specific amino acid depletion, a global decrease of translation can be triggered, resulting in unchanged tRNA loading and translation elongation. Similarly, our combined RP, tRNA, and polysome data suggest that after more than 30 h of fasting, mice can compensate the lack of amino acids by a large global decrease of translation initiation (Fig. 3*B*), possibly through mTORC1/GCN2 (88), making tRNA availability nonlimiting for translation elongation. However, since ribosome profiling signals, and tRNAs, were measured in relative and not absolute amounts, we cannot fully exclude a total decrease of translation elongation rate, aminoacylation, or tRNA levels. Globally, we showed that at steady state, aminoacyl-tRNA patterns and codon usage balance predict ribosome dwell times for some codons.

Codon optimality was shown, in cell culture, to contribute to differential mRNA translation in response to amino acid-depleted media (25). In fasted mice we did not observe a similar effect, probably due to compensation in the in vivo state. However, GC3 bias (i.e., GC bias at position N3 in codons) was different between genes translated in AL and FA mice (Fig. S5*A*). Genes with high GC3 content were shown to provide more targets for DNA methylation than those with low GC3 and to be enriched in stress responsive genes (89). Oxidative stress occurs during fasting/day in mouse and correlates with GC3 content. Nevertheless, the reason for the higher GC3 level in FA compared to AL still needs to be identified.

In conclusion, ribosome DTs, codon usage, tRNA levels, and translation elongation in mammals obey complex relationships. Although a global understanding is still missing, we were able to link both tRNA/codon usage balance and aminoacylation levels with anomalously slow DTs in the P and A site of the ribosome. Probing different ribosome states (e.g., free A site) using RP combined with different drugs (90) or improving the quantification of (aminoacyl-) tRNA through nucleotide modification removal (46) will lead to better understanding of the determinants of translation elongation and consequences on gene expression levels (91).

Materials and Methods

Animal Experiments. Animal studies were approved by the Service Vétérinaire Cantonal (Lausanne, Switzerland) under license VD3613. The 8-wk-old male C57BL6/J mice (Charles River Laboratory) are kept under diurnal lighting conditions (12-h light, 12-h dark) at a temperature of 21 °C ± 2 °C. After a complete night of fasting, the mice were kept without access to food for an additional period for a total of 30 h. During this time period animals were killed every 8 h starting at ZT4. Control animals were kept on ad libitum feeding regimen.

Ribosome Profiling. Samples preparation for RP was performed as described in ref. 53 except for the conditions without cycloheximide (CHX) in which fresh livers were directly lysed in ice-cold lysis buffer without CHX and directly flash-frozen in liquid nitrogen. To limit possible bias due to footprint size selection related to different conformations of the ribosome (39, 74), a larger band was cut on the TBE-gel. Libraries were generated using NEXTflex Small RNA Sequencing Kit v3 (PerkinElmer) following the manufacturer's protocol. Samples were pooled based on the Illumina indices used. Denaturated pools were spiked with 5% PhiX and clustered (loading equivalent to three samples per lane) onto a rapid single-end v2 flow cell at a concentration of 8pM. Libraries were sequenced on a HiSeq 2500 (Illumina) for 50 cycles.

Polysome Profiling. Using the Gradient Master 108 programmable gradient pourer (Biocomp), 17.5 to 50% sucrose gradients were generated in gradient buffer (20 mM Tris-HCl, 150 mM NaCl, 5 mM $MgCl_2$, 1 mM DTT, and 100 μg/mL Cycloheximide). Liver lysates from AL ZT18 and FA ZT18 containing same amount of RNA were then loaded onto sucrose gradients and centrifuged for 3.5 h at 28,000 rpm in an SW40Ti rotor in a Beckman L7 ultracentrifuge (Beckman Coulter). After centrifugation, gradients were fractionated and measured for RNA content (absorbance at 254 nm) using a Piston Gradient Fractionator (Biocomp) connected to a UV monitor (Bio-Rad).

(Aminoacyl-) tRNA Profiling. The tRNA profiling protocol was adapted and modified from ref. 9. We tested the initial protocol on mouse liver samples, but the results showed a high proportion of unspecific ligations between the left and right probes from distinct tRNAs. We solved this issue by inverting the order of two steps in the protocol: we performed the pull-down and cleaning on magnetic beads before the splint ligation between the two DNA probes on the tRNA (Fig. S7*A*). Oxidation of 3′-tRNA by periodate was adapted from ref. 62. All of the steps were performed under cold and acidic conditions to avoid deacylation of the tRNAs before sodium periodate oxidation. For further details, see *SI Appendix*.

Inference of Dwell Times and Translation Fluxes.

Preprocessing of ribosome profiling data. RP datasets from yeast, mouse, and human were mapped on the sacCer3, mm10, and hg38 genomes, respectively, using STAR software (92) with parameters –seedSearchStartLmax 15. Genome indexes were built using Ensembl transcripts annotations. Adapters were retrieved for the different datasets and input as parameters for STAR. In the case of NEXTFlex library, fastqs files were parsed and duplicated sequences (UMI and insert) were removed. Sequences were trimmed for adapters using fastx_clipper with parameters -Q33 -a TGGAATTCTCGGGTGCCAAGG -l 11 and UMIs were removed (four nucleotides on both sides). Then, the fastq files were mapped using STAR with options –seedSearchStartLmax 15. The subsequent BAM files were sorted and indexed.

Read counting on the coding sequences. For each protein coding transcript with a CDS larger than 120 nucleotides, reads with 0 mismatches, unique mapping (nM:i:0 and NH:i:1), and a length between 25 and 40 nucleotides were retrieved using samtools view in the respective region. E site position was defined, for each read size, in function of the frame on the CDS and pileup plots at the start codon. A sliding window of 120 nucleotides moving 3 by 3 on the CDS of protein coding genes were computed, and the respective sequences were reported (Fig. S1*D*). This set of sequences is used as a reference, and their respective number of counts is set to 0. Every time a read occurs at one of these sequences, we incremented the count by 1 (Fig. S1*D*). Sequences with a window spanning the start or stop codon were removed.

Data filtering. Genes with less than 5% of positions covered or fewer than five positions observed were discarded. Genes with fewer than 100 counts were removed. Sequences containing a stop codon (TAG, TGA, or TAA) or that were nonunique in the coding genome were discarded. This filtering typically kept about 5,000 genes in mammals, depending on the sample coverage.

Generalized linear model for ribosome profiling count data.

Model. We used a GLM for the observed RP read counts at the different positions on the gene CDS. Here the read counts Y_{igs} at a specific codon position i corresponding to the ribosome E site on the CDS of a gene g in sample s were modeled as a negative binomial (NB) [i.e., commonly used for overdispersed count data (93)] with mean μ_{igs} and dispersion parameter θ_s.

$$\begin{aligned} Y_{igs} &\sim NB\left(\mu_{igs}, \theta_s\right) \\ \mathrm{E}[Y_{igs}] &= \mu_{igs} \\ \mathrm{Var}\left(Y_{igs}\right) &= \mu_{igs} + \frac{\mu_{igs}^2}{\theta_s} \end{aligned} \qquad [1]$$

SYSTEMS BIOLOGY

The mean is further modeled as follows (omitting the sample index for simplicity):

$$h(\mu_{i,g}) = \underbrace{f_g}_{\text{gene flux}} + \left(\sum_{k=-20}^{20} \underbrace{\tau^{(1)}_{k,c(i+k)}}_{\text{single DTs}} \right) + \underbrace{\tau^{(2)}_{c(i+s1),c(i+s2)}}_{\text{pairs DTs}} + \text{offsets(library size and/or RNA} - \text{Seq)} \quad [2]$$

$$\text{with}(s_1, s_2) \in \begin{cases} (0, 1) \text{ for the E : P fit} \\ (0, 2) \text{ for the E : A fit} \\ (1, 2) \text{ for the P : A fit} \end{cases}$$

Here $c(i) \in \{AAA, AAC, AAG, \ldots, TTT\}$. $h(x) = \log(x)$ is the so-called link function that allows us to express the product of gene flux and DTs (equal to the expected RP density) as a sum in log-space. $\tau^{(1)}_{k,c(i+k)}$ denotes the contributions of single-codon DTs (in log scale) for the 61 sense codons at position k relative to the ribosome E site. $\tau^{(2)}_{c(i+s1),c(i+s2)}$ denotes the contributions of codon pair DTs (again in log scale) for the 61^2 pairs of sense codons at positions (s_1, s_2) relative to the ribosome E site. These codon pair matrices are modeled for the sites E:A, E:P, and P:A one by one. f_g is the gene-specific translation flux (in log scale). Note that since this problem does not have full rank, we must fix some constraints. To best compare DTs across samples, we chose to express the DTs relative to the mean for each site. Specifically, we apply the convention $\sum_c \tau^{(1)}_{k,c} = 0$ for all k, $\sum_c \tau^{(2)}_{c,c'} = 0$ for all c', and $\sum_{c'} \tau^{(2)}_{c,c'} = 0$ for all c and shifted the gene fluxes accordingly. The fit was performed using the *glm4()* function from the R package *MatrixModels* with the noise family *negative.binomial*(θ_s) from the *MASS* package and with sparse design matrix option. The offsets make the gene fluxes normalized by library size. In addition, when specified in the text, we normalized gene translation fluxes by mRNA abundance by fitting the same model to RNA-seq data (since RNA coverage is uniform the DTs then represent sequencing-dependent biases). From the RNA model we predicted the expected gene- and position-specific read counts and used them as an offset term (details in code).

In all figures showing DTs, point estimates as returned by *glm4* and relatively expressed in log are plotted. The reproducibility of those point estimates across biological samples is shown in Fig. S3C. Note that despite the assumptions made, the single-codon DT model, owing to the window of explanatory codons considered, can capture signatures of collided ribosomes in the fitted dwell times, when this resulting stalling has a codon-specific cause, as in the 3-AT condition S2C.

Negative Binomial Noise Model. θ_s was taken as a sample specific parameter and was empirically estimated from the variance-mean relationship expected for a negative binomial (NB) distribution. Specifically, for each gene we used pairs of adjacent codons occurring more than once, the rationale being that according to our steady-state model, the counts observed on multiple positions behave as replicates (i.e., the counts are sampled from the same NB). For those pairs of codons, we computed the respective mean and variance of counts, and since we assumed that θ_s only depends on the sample, we then estimated θ_s globally (from all pairs on all genes) by linear regression using Eq. **1** (Fig. S1*E*).

Differential Expression in Ad Libitum Fed vs. Fasted Mice. Two outlier samples (ZT12/FA/CHX and ZT04/FA/NOCHX) were excluded for the differential expression analysis and DT modeling. Statistics were computed using EdgeR (94) comparing a model including factors for time, feeding, and drug conditions against a model without the feeding term.

Data Availability and Specificity. Sequencing data of this study have been submitted to the National Center for Biotechnology Information (NCBI) Gene Expression Omnibus (GEO), http://www.ncbi.nlm.nih.gov/geo/ (accession no. GSE126384). Datasets and GEO references of publicly available datasets used are: mouse liver tissues (GSE73553, $n = 84$) (53); mouse liver tissues (GSE46038, runs: SRR826795, SRR826796, SRR826797, $n = 3$) (59); Huh7 cells (GSE94454, runs: SRR5227294, SRR5227295, SRR5227296, SRR5227303, SRR5227304, SRR5227305, $n = 6$) (61); *Saccharomyces cerevisiae* (GSE61012, runs: SRR1562907, SRR1562909, SRR1562911, SRR1562913, $n = 4$) (50); mouse kidney tissues (GSE81283, $n = 24$) (60); and *Saccharomyces cerevisiae* dom34 KO/3-AT (GSE52968, runs: SRR1042865, SRR1042866, SRR1042867, $n = 1$) (26).

Code Availability. Codes to model DTs and flux from ribosome profiling are available on GitHub: https://github.com/cgob/codonDT_snakemake.

ACKNOWLEDGMENTS. We thank Nicolas Bonhoure and Stefan Morgenthaler for useful discussions. Research in the F.N. laboratory was supported by the Ecole Polytechnique Federale de Lausanne (EPFL) and by the Swiss National Science Foundation grant 310030_173079 to F.N. Some computations were performed on the Vital-It computing platform and the facilities of the Scientific IT and Application Support Center of EPFL.

1. C. Gobet, F. Naef, Ribosome profiling and dynamic regulation of translation in mammals. *Curr. Opin. Genet. Dev.* **43**, 120–127 (2017).
2. A. G. Hinnebusch, J. R. Lorsch, The mechanism of eukaryotic translation initiation: New insights and challenges. *Cold Spring Harbor Perspect. Biol.* **4**, a011544 (2012).
3. C. E. Brule, E. J. Grayhack, Synonymous codons: Choose wisely for expression. *Trends Genet.* **33**, 283–297 (2017).
4. V. Presnyak *et al.*, Codon optimality is a major determinant of mRNA stability. *Cell* **160**, 1111–1124 (2015).
5. A. Radhakrishnan *et al.*, The DEAD-box protein Dhh1p couples mRNA decay and translation by monitoring codon optimality. *Cell* **167**, 122–132.e9 (2016).
6. V. Pelechano, W. Wei, L. M. Steinmetz, Widespread co-translational RNA decay reveals ribosome dynamics. *Cell* **161**, 1400–1412 (2015).
7. C. H. Yu *et al.*, Codon usage influences the local rate of translation elongation to regulate co-translational protein folding. *Mol. Cell* **59**, 744–754 (2015).
8. D. Chu *et al.*, Translation elongation can control translation initiation on eukaryotic mRNAs. *EMBO J.* **33**, 21–34 (2014).
9. H. Goodarzi *et al.*, Modulated expression of specific tRNAs drives gene expression and cancer progression. *Cell* **165**, 1416–1427 (2016).
10. F. Loayza-Puch *et al.*, Tumour-specific proline vulnerability uncovered by differential ribosome codon reading. *Nature* **530**, 490–494 (2016).
11. F. Rapino *et al.*, Codon-specific translation reprogramming promotes resistance to targeted therapy. *Nature* **558**, 605–609 (2018).
12. S. Varenne, J. Buc, R. Lloubes, C. Lazdunski, Translation is a non-uniform process. *J. Mol. Biol.* **180**, 549–576 (1984).
13. A. Dana, T. Tuller, The effect of tRNA levels on decoding times of mRNA codons. *Nucleic Acids Res.* **42**, 9171–9181 (2014).
14. T. E. Quax, N. J. Claassens, D. Söll, J. van der Oost, Codon bias as a means to fine-tune gene expression. *Mol. Cell* **59**, 149–161 (2015).
15. M. A. Sørensen, S. Pedersen, Absolute in vivo translation rates of individual codons in Escherichia coli. The two glutamic acid codons GAA and GAG are translated with a threefold difference in rate. *J. Mol. Biol.* **222**, 265–280 (1991).
16. N. T. Ingolia, L. F. Lareau, J. S. Weissman, Ribosome profiling of mouse embryonic stem cells reveals the complexity and dynamics of mammalian proteomes. *Cell* **147**, 789–802 (2011).
17. S. van Heesch *et al.*, The translational landscape of the human heart. *Cell* **178**, 242–260 (2019).
18. N. T. Ingolia, Ribosome footprint profiling of translation throughout the genome. *Cell* **165**, 22–33 (2016).
19. C. Pop *et al.*, Causal signals between codon bias, mRNA structure, and the efficiency of translation and elongation. *Mol. Syst. Biol.* **10**, 770 (2014).
20. P. B. F. O'Connor, D. E. Andreev, P. V. Baranov, Comparative survey of the relative impact of mRNA features on local ribosome profiling read density. *Nat. Commun.* **7**, 12915 (2016).
21. H. Fang *et al.*, Scikit-ribo enables accurate estimation and robust modeling of translation dynamics at codon resolution. *Cell Syst.* **6**, 180–191.e4 (2018).
22. R. Tunney *et al.*, Accurate design of translational output by a neural network model of ribosome distribution. *Nat. Struct. Mol. Biol.* **25**, 577–582 (2018).
23. C. A. Charneski, L. D. Hurst, Positively charged residues are the major determinants of ribosomal velocity. *PLoS Biol.* **11**, e1001508 (2013).
24. A. M. Darnell, A. R. Subramaniam, E. K. O'Shea, Translational control through differential ribosome pausing during amino acid limitation in mammalian cells. *Mol. Cell* **71**, 229–243 (2018).
25. M. Saikia *et al.*, Codon optimality controls differential mRNA translation during amino acid starvation. *RNA* **22**, 1719–1727 (2016).
26. N. R. Guydosh, R. Green, Dom34 rescues ribosomes in 3′ untranslated regions. *Cell* **156**, 950–962 (2014).
27. D. D. Nedialkova, S. A. Leidel, Optimization of codon translation rates via tRNA modifications maintains proteome integrity. *Cell* **161**, 1606–1618 (2015).
28. F. Tuorto *et al.*, The tRNA methyltransferase Dnmt2 is required for accurate polypeptide synthesis during haematopoiesis. *EMBO J.* **34**, 2350–2362 (2015).
29. H. J. Chou, E. Donnard, H. T. Gustafsson, M. Garber, O. J. Rando, Transcriptome-wide analysis of roles for tRNA modifications in translational regulation. *Mol. Cell* **68**, 978–992 (2017).
30. C. Pop *et al.*, Causal signals between codon bias, mRNA structure, and the efficiency of translation and elongation. *Mol. Syst. Biol.* **10**, 770(2014).
31. S. Zhang *et al.*, Analysis of ribosome stalling and translation elongation dynamics by deep learning. *Cell Systems* **5**, 212–220 (2017).
32. T. E. Gorochowski, Z. Ignatova, R. A. L. Bovenberg, J. A. Roubos, Trade-offs between tRNA abundance and mRNA secondary structure support smoothing of translation elongation rate. *Nucleic Acids Res.* **43**, 3022–3032 (2015).
33. K. Döring *et al.*, Profiling Ssb-nascent chain interactions reveals principles of Hsp70-assisted folding. *Cell* **170**, 298–311 (2017).

34. Y. Harigaya, R. Parker, The link between adjacent codon pairs and mRNA stability. *BMC Genom.* **18**, 364 (2017).
35. C. E. Gamble, C. E. Brule, K. M. Dean, S. Fields, E. J. Grayhack, Adjacent codons act in concert to modulate translation efficiency in yeast. *Cell* **166**, 679–690 (2016).
36. K. D. Duc, Y. S. Song, The impact of ribosomal interference, codon usage, and exit tunnel interactions on translation elongation rate variation. *PLoS Genet.* **14**, e1007166 (2018).
37. J. Gardin *et al.*, Measurement of average decoding rates of the 61 sense codons in vivo. *eLife* **3**, e03735 (2014).
38. F. Aeschimann, J. Xiong, A. Arnold, C. Dieterich, H. Großhans, Transcriptome-wide measurement of ribosomal occupancy by ribosome profiling. *Methods* **85**, 75–89 (2015).
39. L. F. Lareau, D. H. Hite, G. J. Hogan, P. O. Brown, Distinct stages of the translation elongation cycle revealed by sequencing ribosome-protected mRNA fragments. *eLife* **3**, e01257 (2014).
40. C. D. S. Duncan, J. Mata, Effects of cycloheximide on the interpretation of ribosome profiling experiments in Schizosaccharomyces pombe. *Sci. Rep.* **7**, 1–11 (2017).
41. M. V. Gerashchenko, A. V. Lobanov, V. N. Gladyshev, Genome-wide ribosome profiling reveals complex translational regulation in response to oxidative stress. *Proc. Natl. Acad. Sci. U.S.A.* **109**, 17394–17399 (2012).
42. J. A. Hussmann, S. Patchett, A. Johnson, S. Sawyer, W. H. Press, Understanding biases in ribosome profiling experiments reveals signatures of translation dynamics in yeast. *PLoS Genet.* **11**, e1005732 (2015).
43. A. Bartholomäus, C. D. Campo, Z. Ignatova, Mapping the non-standardized biases of ribosome profiling. *Biol. Chem.* **397**, 23–35 (2016).
44. T. E. Quax, N. J. Claassens, D. Söll, J. van der Oost, Codon bias as a means to fine-tune gene expression. *Mol. Cell* **59**, 149–161 (2015).
45. A. Orioli, tRNA biology in the omics era: Stress signalling dynamics and cancer progression. *Bioessays* **39**, 1600158 (2017).
46. G. Zheng *et al.*, Efficient and quantitative high-throughput tRNA sequencing. *Nat. Methods* **12**, 835–837 (2015).
47. T. Gogakos *et al.*, Characterizing expression and processing of precursor and mature human tRNAs by hydro-tRNAseq and PAR-CLIP. *Cell Rep.* **20**, 1463–1475 (2017).
48. A. E. Cozen *et al.*, ARM-seq: AlkB-facilitated RNA methylation sequencing reveals a complex landscape of modified tRNA fragments. *Nat. Methods* **12**, 879–884 (2015).
49. M. E. Evans, W. C. Clark, G. Zheng, T. Pan, Determination of tRNA aminoacylation levels by high-throughput sequencing. *Nucleic Acids Res.* **45**, e133–e133 (2017).
50. C. H. Jan, C. C. Williams, J. S. Weissman, Principles of ER cotranslational translocation revealed by proximity-specific ribosome profiling. *Science* **346**, 1257521–1257521 (2014).
51. M. Y. Pavlov, *et al.*, Slow peptide bond formation by proline and other N-alkylamino acids in translation. *Proc. Natl. Acad. Sci. U.S.A.* **106**, 50–54 (2009).
52. N. T. Ingolia, J. A. Hussmann, J. S. Weissman, Ribosome profiling: Global views of translation. *Cold Spring Harbor Perspect. Biol.* **11**, a032698 (2019).
53. F. Atger *et al.*, Circadian and feeding rhythms differentially affect rhythmic mRNA transcription and translation in mouse liver. *Proc. Natl. Acad. Sci. U.S.A.* **112**, E6579–E6588 (2015).
54. A. González, M. N. Hall, Nutrient sensing and TOR signaling in yeast and mammals. *EMBO J.* **36**, 397–408 (2017).
55. E. Gutierrez *et al.*, eIF5A promotes translation of polyproline motifs. *Mol. Cell* **51**, 35–45 (2013).
56. A. Lecanda *et al.*, Dual randomization of oligonucleotides to reduce the bias in ribosome-profiling libraries. *Methods* **107**, 89–97 (2016).
57. M. V. Gerashchenko, V. N. Gladyshev, Translation inhibitors cause abnormalities in ribosome profiling experiments. *Nucleic Acids Res.* **42**, e134 (2014).
58. F. Zhang, X. Xu, B. Zhou, Z. He, Q. Zhai, Gene expression profile change and associated physiological and pathological effects in mouse liver induced by fasting and refeeding. *PloS One* **6**, e27553 (2011).
59. M. T. Howard, B. A. Carlson, C. B. Anderson, D. L. Hatfield, Translational redefinition of UGA codons is regulated by selenium availability. *J. Biol. Chem.* **288**, 19401–19413 (2013).
60. V. Castelo-Szekely, A. B. Arpat, P. Janich, D. Gatfield, Translational contributions to tissue specificity in rhythmic and constitutive gene expression. *Genome Biol.* **18**, 116 (2017).
61. N. G. Lintner *et al.*, Selective stalling of human translation through small-molecule engagement of the ribosome nascent chain. *PLoS Biol.* **15**, e2001882 (2017).
62. K. A. Dittmar, M. A. Sørensen, J. Elf, M. Ehrenberg, T. Pan, Selective charging of tRNA isoacceptors induced by amino-acid starvation. *EMBO Rep.* **6**, 151–157 (2005).
63. T. M. Lowe, P. P. Chan, tRNAscan-SE On-line: integrating search and context for analysis of transfer RNA genes. *Nucleic Acids Res.* **44**, W54–W57 (2016).
64. D. Canella *et al.*, A multiplicity of factors contributes to selective RNA polymerase III occupancy of a subset of RNA polymerase III genes in mouse liver. *Genome Res.* **22**, 666–680 (2012).
65. K. A. Dittmar, J. M. Goodenbour, T. Pan, Tissue-specific differences in human transfer RNA expression. *PLoS Genet.* **2**, e221 (2006).
66. S. Mahlab, T. Tuller, M. Linial, Conservation of the relative tRNA composition in healthy and cancerous tissues. *RNA* **18**, 640–652 (2012).
67. K. L. M. Rudolph *et al.*, Codon-driven translational efficiency is stable across diverse mammalian cell states. *PLoS Genet.* **12**, 1–23 (2016).
68. S. Pechmann, J. Frydman, Evolutionary conservation of codon optimality reveals hidden signatures of cotranslational folding. *Nat. Struct. Mol. Biol.* **20**, 237–243 (2013).
69. C. J. Woolstenhulme, N. R. Guydosh, R. Green, A. R. Buskirk, High-precision analysis of translational pausing by ribosome profiling in bacteria lacking EFP. *Cell Rep.* **11**, 13–21 (2015).
70. F. F. V. Chevance, K. T. Hughes, Case for the genetic code as a triplet of triplets. *Proc. Natl. Acad. Sci. U.S.A.* **114**, 4745–4750 (2017).
71. S. Kanaya, Y. Yamada, Y. Kudo, T. Ikemura, Studies of codon usage and tRNA genes of 18 unicellular organisms and quantification of Bacillus Subtilis tRNAs: Gene expression level and species-specific diversity of codon usage based on multivariate analysis. *Gene* **238**, 143–155 (1999).
72. P. Tesina *et al.*, Molecular mechanism of translational stalling by inhibitory codon combinations and poly(A) tracts. *EMBO J.*, 755652 (2019).
73. N. T. Ingolia, Ribosome profiling: New views of translation, from single codons to genome scale. *Nat. Rev. Genet.* **15**, 205–213 (2014).
74. F. Mohammad, C. J. Woolstenhulme, R. Green, A. R. Buskirk, Clarifying the translational pausing landscape in bacteria by ribosome profiling. *Cell Rep.* **14**, 686–694 (2016).
75. F. Mohammad, R. Green, A. R. Buskirk, A systematically-revised ribosome profiling method for bacteria reveals pauses at single-codon resolution. *eLife* **8**, 399–404 (2019).
76. P. F. Agris *et al.*, Celebrating wobble decoding: Half a century and still much is new. *RNA Biol.* **15**, 537–553 (2018).
77. S. Alkatib *et al.*, The contributions of wobbling and superwobbling to the reading of the genetic code. *PLoS Genet.* **8**, e1003076 (2012).
78. J. R. Yang, X. Chen, J. Zhang, Codon-by-codon modulation of translational speed and accuracy via mRNA folding. *PLoS Biol.* **12**, e1001910 (2014).
79. M. Stadler, A Fire, Wobble base-pairing slows in vivo translation elongation in metazoans. *RNA* **17**, 2063–2073 (2011).
80. M. Lubas *et al.*, eIF5A is required for autophagy by mediating ATG3 translation. *EMBO Rep.* **19** e46072 (2018).
81. V. Pelechano, P. Alepuz, eIF5A facilitates translation termination globally and promotes the elongation of many non polyproline-specific tripeptide sequences. *Nucleic Acids Res.* **45**, 7326–7338 (2017).
82. R. Shalgi *et al.*, Widespread regulation of translation by elongation pausing in heat shock. *Mol. Cell* **49**, 439–452 (2013).
83. P. Somogyi, A. J. Jenner, I. Brierley, S. C. Inglis, Ribosomal pausing during translation of an RNA pseudoknot. *Mol. Cell Biol.* **13**, 6931–40 (1993).
84. J. Tholstrup, L. B. Oddershede, M. A. Sørensen, MRNA pseudoknot structures can act as ribosomal roadblocks. *Nucleic Acids Res.* **40**, 303–313 (2012).
85. S. Juszkiewicz *et al.*, ZNF598 is a quality control sensor of collided ribosomes. *Mol. Cell* **72**, 469–481 (2018).
86. C. L. Simms, L. L. Yan, H. S. Zaher, Ribosome collision is critical for quality control during no-go decay. *Mol. Cell* **68**, 361–373 (2017).
87. A. B. Arpat *et al.*, Transcriptome-wide sites of collided ribosomes reveal principles of translational pausing. bioRxiv:10.1101/710061 (22 July 2019).
88. R. L. Wolfson, D. M. Sabatini, The dawn of the age of amino acid sensors for the mTORC1 pathway. *Cell Metabol.* **26**, 301–309 (2017).
89. T. V. Tatarinova, N. N. Alexandrov, J. B. Bouck, K. A. Feldmann, GC3biology in corn, rice, sorghum and other grasses. *BMC Genom.* **11**, 308 (2010).
90. C. C. C. Wu, B. Zinshteyn, K. A. Wehner, R. Green, High-resolution ribosome profiling defines discrete ribosome elongation states and translational regulation during cellular stress. *Mol. Cell* **73**, 959–970.e5 (2019).
91. Q. Wu *et al.*, Translation affects mRNA stability in a codon-dependent manner in human cells. *eLife* **8**, 1–22 (2019).
92. A. Dobin *et al.*, STAR: Ultrafast universal RNA-seq aligner. *Bioinformatics* **29**, 15–21 (2013).
93. M. I. Love, W. Huber, S. Anders, Moderated estimation of fold change and dispersion for RNA-seq data with DESeq2. *Genome Biol.* **15**, 1–21 (2014).
94. M. D. Robinson, D. J. Mccarthy, G. K. Smyth, edgeR: A Bioconductor package for differential expression analysis of digital gene expression data. *Bioinformatics* **26**, 139–140 (2010).